THE JOURNAL OF PHYSICAL CHEMISTRY C

pubs.acs.org/JPCC Article

Insulator–Metal Transition in the Nd_2CoFeO_6 Disordered Double Perovskite

Leonardo S. de Oliveira, Fernando P. Sabino, Daniel Z. de Florio, Anderson Janotti, Gustavo M. Dalpian, and Jose A. Souza*

Cite This: J. Phys. Chem. C 2020, 124, 22733–22742 Read Online

ACCESS | Metrics & More | Article Recommendations | Supporting Information

ABSTRACT: A comprehensive study on the correlations of structural, magnetic, and electronic properties of a new disordered Nd_2CoFeO_6 double perovskite has been conducted. The lack of strong divergence of the magnetic susceptibility suggests competition between magnetic interactions at the magnetic phase transition T_N = 246 K, which is confirmed by the absence of a heat capacity peak. The magnetic susceptibility results indicate that the Fe/Co spins form a classical noninteracting paramagnetic state above $T \approx 2.2T_N$, while deviations are found at intermediate temperatures indicating the presence of strong short-range magnetic interactions. AC and DC electrical resistivity results reveal a melting of insulating polaronic behavior to a metallic-like conductivity, establishing an electronic crossover closely related to both local magnetic moment and lattice-parameter evolution. We show from density functional calculations that the magnetic configurations have a strict relation to this crossover, being associated to a transition from low to high spin states of Co^{3+} ions. This insulator–metal transition has its origin driven by a local increase in the magnetic moment of Co^{3+} ions. Our results point to a scenario in which a continuous spin-state transition triggers a crossover between distinct electronic states from the insulating polaronic behavior to permanent metallic states.

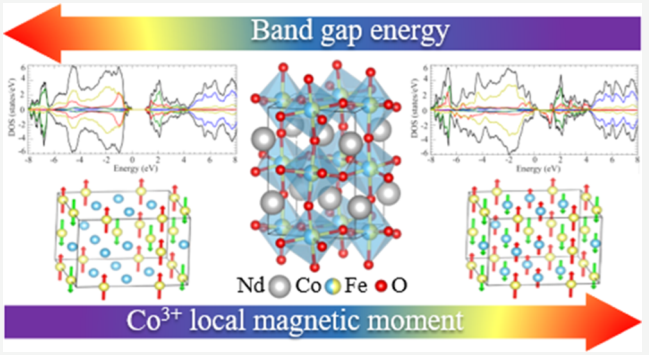

1. INTRODUCTION

Describing the microscopic mechanism underlying electronic, structural, and magnetic phase transitions in strong spin-lattice-charge coupled systems is a fundamental challenge that has attracted great interest in condensed matter physics.[1] Doped transition metal oxides exhibiting coexistence of strong correlations among charge, lattice, orbital, and magnetic orderings are systems where a complex magnetic and electrical phase diagram can lead to novel physical phenomena. The introduction of structural disorder brought about by random distribution of different local atoms in the crystal lattice can strongly influence the degrees of freedom of electrons. Double exchange magnetic interactions and electron-lattice coupling theories are usually proposed for ferromagnetic metallic couplings, but a better understanding on the correlations between magnetism and electronic charge transport is still missing for superexchange disordered systems.[2]

Double perovskite compounds with $A_2BB'O_6$ formula (where A = alkaline earth or rare-earth metal, B and B′ = transition metal) are suitable materials to explore all of these degrees of freedom.[3] The strong correlated unusual charge transport and magnetic properties bring about additional useful functionalities.[4−6] An additional degree of complexity in the structure property relationship is introduced when a random assembly of BO_6 and $B'O_6$ octahedra is considered in the crystal field. The introduced chemical disorder, also known as antisite disorder (ASD),[7] can suppress or even lead to different magnetic and electronic phases into the system.[8,9] Interestingly, in the disordered Ln_2CoFeO_6 family it has been observed multiple magnetic and electrical properties leading to high thermoelectric figure-of-merit,[10] spin reorientation transitions,[11−13] spin canting,[14] pyroelectric current,[13] magnetic entropy change,[15,16] and Griffith's-like phase.[17] From all of these results, it seems natural that spin-charge-lattice interactions play an essential role on the observed complex magnetic and electrical phase diagram. However, the origin of the different magnetic and electronic phases as temperature changes is not clear because of the lack of systematic studies on the fundamental properties of these systems. Although a variety of different physical phenomena have been observed in these systems, setting a correlation among them is not usually

Received: August 19, 2020
Revised: September 15, 2020
Published: September 16, 2020

https://dx.doi.org/10.1021/acs.jpcc.0c07585
J. Phys. Chem. C 2020, 124, 22733–22742

available. Thermally induced electronic state transitions occurring at each magnetic and electronic phase gives a further ingredient to the problem. More specifically, owing to the disordered nature, a detailed understanding of its paramagnetic (PM) spin configuration is usually missing in both experimental and theoretical viewpoints.

The variety of unusual physical phenomena observed in these system makes them good prototypes for studying the correlation of spin states with unique magnetic short-range ordering and possible appearance of insulator−metal (IM) transitions. In this work, we report Nd_2CoFeO_6 as a novel disordered double perovskite compound with a metallic high temperature paramagnetic phase. Structural, magnetic, and electronic transport characterizations along with first-principles-based special quasirandom structures (SQS) simulations were carried out to understand the role of the magnetic lattice and spin-state distribution in the IM transition. AC and DC electrical resistivity measurements show a transition from the insulating polaronic behavior to a metallic behavior, unambiguously establishing an electronic crossover at high temperatures, which is attributed to a transition from low spin to high spin state of the Co^{3+} ions. Our results point to a scenario in which a continuous spin-state transition triggers the crossover between distinct electronic states, from insulating polaron-like to overlapping metallic states.

2. EXPERIMENTAL AND THEORETICAL APPROACHES

Polycrystalline Nd_2CoFeO_6 sample was prepared by a conventional solid−state reaction route with high purity (99.99%) starting materials. Stoichiometric amounts of Nd_2O_3, Fe_2O_3, and Co_3O_4 were mixed and ground together in a mortar and preheated at 1000 °C in air for 24 h in alumina crucibles. Further, the powder was regrounded, pelletized, and then heat treated for 24 h at 1300 °C, followed by a slow cooling rate of 1 K/min to room temperature. It is important to point out that because of the basic sites of rare-earth oxides, the raw Nd_2O_3 was previously calcined at 700 °C in order to eliminate impurities (see the Supporting Information, Figure S1).

The crystalline phase identification was analyzed by X-ray diffraction (XRD) on a STOE STADI-P diffractometer using MoK_α radiation (λ = 0.7093 Å) in Debye−Scherrer geometry equipped with curved a Ge(111) monochromator. Unit-cell parameters were refined through the Rietveld method[18] in GSAS software package[19] following the IUCr recommendations.[20] Low temperature heat capacity was measured in the physical property measurement system (PPMS). DC Magnetization measurements were carried out using a magnetic property measurement system (MPMS) SQUID magnetometer from Quantum Design. Temperature-dependent magnetization was measured under zero field cooled (ZFC) and field cooled (FC) procedures. Magnetic field dependence of magnetization was collected at selected temperatures. High temperature impedance spectroscopy measurements were carried out up to ≈1200 K in air, under steady-state conditions, with a Solatron 1260 Frequency Response Analyzer.

Our first-principles calculations are based on the density functional theory (DFT) as implemented in the Vienna *Ab*-initio Simulation Package (VASP).[21,22] For the exchange and correlation, we employed the Perdew−Burke−Ernzerhof revised for solids (PBESol) functional, which leads to an accurate description of structural and electronic properties of the system that is subject to the present study.[23] To describe the interaction between the ionic cores and the valence electrons we used the projected augmented waves (PAW) method,[24,25] with the following valence configurations: O ($2s^2$ $2p^4$), Fe ($3d^6$ $4s^2$), Co ($3d^7$ $4s^2$), Nd ($5s^2$ $5p^6$ $4f^1$ $6s^2$).[24,25] Three of four f-electrons of Nd were considered as core electrons, given the weak interaction with the local magnetic moment of the individual Fe and Co atoms. Test calculation with all valence f-electrons and with three core and one valence f-electrons lead to similar results for Nd_2CoFeO_6, yet treating three Nd f-electrons in the core improves convergence of the calculations.

To minimize the self-interaction errors and improve the description of the magnetic properties, an additional Hubbard term as formulated by Dudarev *et. al.*[26] is included. This is a rotational invariant method, where only the difference between the Coulomb (U) and the exchange (J) parameter is relevant and is determined by the effective potential U_{eff} parameter. We set U_{eff} = 4 eV for the d states of Fe and Co. To minimize the forces in each atom and the stress tensor, we used a plane waves energy cutoff of 600 eV within the PBESol + U. For the Brillouin zone integrations, a k-points mesh of 5 × 4 × 3 was employed for the double perovskite primitive cell with 20 atoms, and the same k-points density was used for all of the supercells. To compute the electronic properties, such as the density of states (DOS), the k-mesh density was doubled. The Nd_2CoFeO_6 compound was constructed using a supercell, which is a 2 × 2 × 1 repetition of the orthorhombic structure of the $NdFeO_3$ cell, resulting in a cell with 80 atoms. Based on the experimental evidences that the Co and Fe atoms are disorderly distributed on the B-sites, the Nd_2CoFeO_6 compound was simulated using a SQS.[27,28] In addition, an SQS was also used to determine the magnetic moment configuration in the supercell for the PM phase.[29] The total magnetic moment of the supercell was constrained to be zero, maintaining an equal amount of spin up and down for each chemical species.

3. RESULTS AND DISCUSSION

3.1. Nd_2CoFeO_6 Crystal Structure. Obtaining single crystalline phase of double perovskite has proved to be challenging. Here, polycrystalline Nd_2CoFeO_6 samples were successfully obtained by the solid−state reaction method. The XRD pattern and the Rietveld refinement, at room temperature, for Nd_2CoFeO_6 are shown in Figure 1a. The sharp Bragg reflections and the absence of additional peaks indicate the growth of a single phase with high crystallinity, without traces of impurities or incomplete reactions. Structural Rietveld refinement reveals that the compound deviates from the ideal cubic structure, owing an orthorhombic *Pnma* space group symmetry (no. 62) with tilted octahedra. A schematic representation of its crystal structure is shown in the inset of Figure 1a. In this structure, the indistinguishable occupation of Fe and Co ions at 4b Wyckoff sites, as well as the absence of superstructure reflections are fingerprints of the disordered double perovskite structure. Unfortunately, the XRD source cannot distinguish Fe and Co transition-metal ions at the 4b sites[30,31] because of the similar atomic scattering factors. For this reason, the occupancy factor was kept constant and half-occupied by both transition metals. The refined unit-cell parameters from room temperature XRD are listed in Table 1.

We have also studied possible changes in the crystal structure as a function of temperature. The temperature dependence of the lattice parameters is shown in Figure 1b. A

https://dx.doi.org/10.1021/acs.jpcc.0c07585
J. Phys. Chem. C 2020, 124, 22733−22742

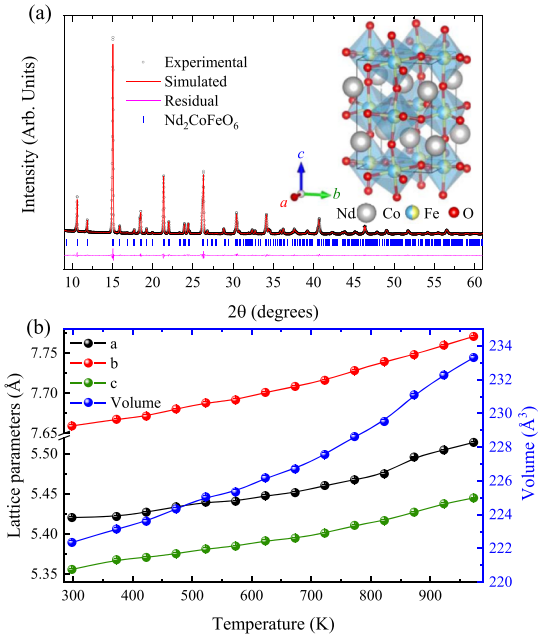

Figure 1. (a) Room temperature XRD pattern along with Rietveld refinement for Nd_2CoFeO_6. The tickmarks indicate the Bragg reflections for *Pnma* space group symmetry. The inset shows the crystal structure of Nd_2CoFeO_6 with disordered and tilted octahedra. (b) Temperature dependent unit-cell parameters obtained thought Rietveld refinement.

Table 1. Room Temperature Structural Parameters of Nd_2CoFeO_6[a]

atom	site	*x*	*y*	*z*	Occ.	U_{iso}
Nd	4c	0.541	0.25	0.507	1	0.008
Fe	4b	0.5	0	0	0.5	0.009
Co	4b	0.5	0	0	0.5	0.009
O1	4c	−0.01	0.25	0.426	1	0.018
O2	8d	0.289	0.037	0.710	1	0.005

[a]Unit-cell parameters: *a* (Å) = 5.4333(1), *b* (Å) = 7.6326(2), *c* (Å) = 5.3846(1). R_{WP} = 0.005 and R_P = 0.044.

nonlinear behavior is observed for the volumetric expansion of Nd_2CoFeO_6, which is not followed by a structural phase transition. A careful analysis around 825 K reveals a small step in the *a*-axix. We will show that this feature emerges as an evidence of lattice-spin coupling, which will have strong influence on the charge transport, as discussed later.

3.2. Magnetic Susceptibility and Spin-Ordering Simulations. The magnetic susceptibility as a function of temperature under selected magnetic fields is shown in Figure 2a. At low temperatures, a broad peak at $T_{SR} \approx 34$ K is observed, which vanishes as the applied magnetic field increases up to 5 kOe. The nature of this peak might be related to spin reorientation of Fe^{3+} magnetic moments as observed in several compounds containing Nd−Fe interactions.[32] Below T_{SR}, the magnetization tends to increase, which suggests an induced short-range magnetization of Nd^{3+} sublattice. At intermediate temperatures, we observe an increase in magnetization suggesting a possible critical magnetic ordering temperature of $T_N \approx 246$ K (defined as the maximum inflection of $dM(T)/dT$). The lack of strong divergence of the magnetic correlation at T_N may suggest competition of magnetic interactions, which in some cases can

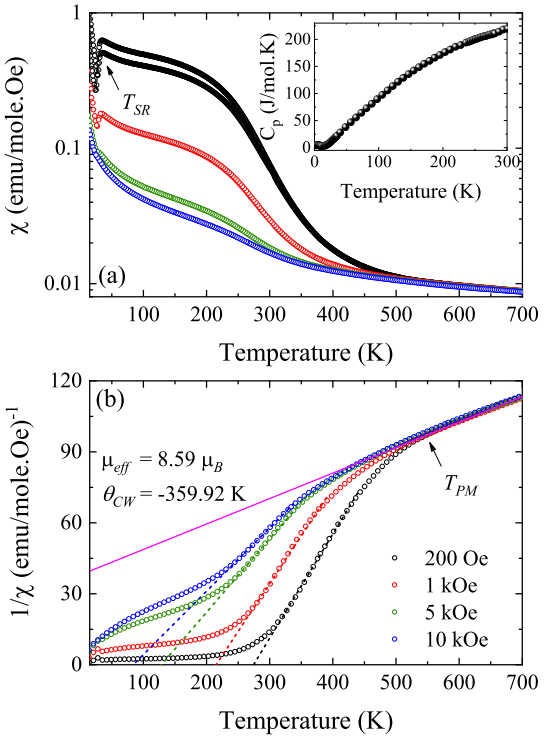

Figure 2. (a) Temperature dependence of magnetic susceptibility shown in logarithm scale for a better data visualization at high temperature. The insert shows the molar heat capacity as a function of temperature. (b) Inverse of magnetic susceptibility under selected magnetic fields. A linear fitting at the low temperature regime, straight dashed lines, reveals a magnetic field dependence. The CW law linear high temperature fitting indicates the conventional PM state.

lead to a complete suppression of the magnetic phase transition. This critical regime has been observed in the same temperature range for Ln_2CoFeO_6 (Ln = Sm, Eu, Dy, Ho, Pr) family (246−269 K), but lower than the simple $LnFeO_3$ (above 600 K).[12,13,15−17] This system shows a very little deviation from the mean-field approach with a frustration index $f = |\theta_{CW}|/T_N$ around 1.4.

In order to shed light on a possible magnetic ordering, it is also important to correlate the observed magnetic transitions with molar heat capacity. The results of heat capacity measurements are shown in the inset of Figure 2a. At low temperature, the main observed feature is a broad Schottky-type anomaly at $T_{Nd} \approx 4.23$ K arising from an induced cooperative magnetic ordering of the Nd^{3+} sublattice.[33] Usually, long-range cooperative magnetic ordering is revealed by the occurrence of a λ-like peak closely related to the critical temperature, which indicates that a conventional thermodynamic phase transition is accompanied by changes in entropy. The results reveal the absence of a conventional phase transition close to $T_N \approx 246$ K, that is, the entropy is not removed when the disordered PM phase changes to an ordered magnetic state. Interestingly, structural disorder caused by the presence of random local strain fields promotes competition between magnetic interactions suppressing the expected peak in the molar heat capacity measurements.[34]

In addition, isothermal magnetization curves were performed for some selected temperatures as shown in Figure S2a. As expected, the magnetization does not show any sign of saturation at high fields, which indicates that the main magnetic fluctuations are antiferromagnetic (AFM). Moreover,

https://dx.doi.org/10.1021/acs.jpcc.0c07585
J. Phys. Chem. C 2020, 124, 22733−22742

at low temperatures and low magnetic fields, the system presents a small hysteresis that may arise from weak ferrimagnetic or ferromagnetic (FM) clusters.[35] Figure S2b shows a nonlinear magnetic contribution that opens a coercive field and remanence, as the temperature decreases, suggesting weak FM interactions. Also, the observed temperature variation of the coercive field indicates the absence of a conventional magnetic phase transition.

The inverse of the magnetic susceptibility as a function of temperature is shown in Figure 2b. Interestingly, a strong deviation from Curie−Weiss (CW) susceptibility is observed in the $T_N < T < T_{PM}$ range, which is indicative of short-range magnetic interactions. As far as the short-range magnetic interaction is concerned, we have studied the CW law within two different temperature intervals above and below $T_{PM} \approx 2.2T_N$. The nature of this deviation from linearity in Curie−Weiss law has been interpreted by using different scenarios including, a two-population model,[36,37] Griffiths-like phase,[38−40] spin-state crossover,[41] ferromagnetic polarons[42] as well the presence of ASD. A closer look in this region shows that the molecular field approach fails if one considers the CW parameters. From the dashed lines in Figure 2b, it was observed that θ_{CW} would yield positive values, indicating that the main magnetic interactions are FM, with an effective magnetic moment of $\mu_{eff} = 4.25\ \mu_B$ at 200 Oe. As the applied magnetic field increases, the slope decreases pointing to a scenario where the Curie constant and θ_{CW} are field dependent. In this sense, at 10 kOe the effective magnetic moment is less than 5.53 μ_B, indicating that a high degree of ASD plays a role in reducing the expected μ_{eff} in this region with the Co^{3+} ions in low spin state, and the weak FM component comes from a coupling of Fe^{3+} clusters.[43]

A linear behavior in the inverse of magnetic susceptibility is reached only for $T > T_{PM}$, revealing the presence of a conventional noninteracting PM state in this region. The effective magnetic moment obtained above T_{PM} corresponds to $\mu_{eff} = 8.59\ \mu_B$ yielding a $\theta_{CW} = -359.92$ K, further indicating a predominance of stronger AFM interactions. The total expected effective magnetic moment $\mu = \sqrt{2\mu_{Nd}^2 + \mu_{Fe}^2 + \mu_{Co}^2}$ is listed in Table 2. For this analysis, we take into account high spin (HS), intermediate spin (IS), and low spin (LS) states for Co^{3+} ions while holding Nd^{3+} and Fe^{3+} in high spin states. These assumptions are supported by the fact that one of the major characteristics of $LnCoO_3$-based compounds is that the transition to a PM state involves a thermally driven spin-state (SS) crossover of Co^{3+} ions, indicating an alternate ordering from diamagnetic ground-state with LS state configuration ($t_{2g}^6e_g^0$; $S = 0$) to an excited IS state ($t_{2g}^5e_g^1$; $S = 1$) or to a HS state ($t_{2g}^4e_g^2$; $S = 2$). These fluctuations in the spin-state degeneracy are possible because the crystal-field splitting between t_{2g} and e_g levels is close in energy to the Hund's exchange coupling, therefore thermal perturbations induces electronic transfer to e_g orbitals, which increases the populations of excited Co^{3+} states.[44−46] The obtained $\mu_{eff} = 8.59\ \mu_B$ is slightly smaller than expected for the complete Co^{3+}(HS) and Fe^{3+} (HS) configurations, which is 9.23 μ_B. This difference in experimental and expected result can be understood by considering two possible scenarios involving the coexistence of Co^{3+} ions with different spin states: a mixture containing LS and HS with 52.19% in the high spin state, or a system containing IS and HS with 71% in the intermediate spin state. Both scenarios are feasible and suggest that thermal fluctuations can set the stage for the coexistence of different spin states of Co^{3+} ions. Indeed, the coexistence of different spin states have been reported to strongly influence not only magnetization but also the electronic transport properties.[47−52]

Table 2. Expected Effective Magnetic Moment for Nd_2CoFeO_6[a]

Nd^{3+} (μ_{Fe})		Fe^{3+} (μ_{Fe})		Co^{3+} (μ_{Co})		μ (μ_B)
HS	3.62	HS	5.92	HS	4.90	9.23
				IS	2.82	8.32
				LS	0.00	5.53

[a]The μ values was estimated by holding Nd^{3+} and Fe^{3+} in HS states, while different spin states configurations for Co^{3+} ions were taken into account.

In order to simulate the PM and ordered states, the refined crystal structure was used as a base model to construct a Nd_2CoFeO_6 supercell for our first-principles calculations. The SQS method was employed to distribute the Fe and Co atoms in a supercell with 80 atoms of this disordered compound. The ground state belongs to an AFM configuration with G-type ordering, with lattice parameter of $a = 5.57$ Å, $b = 7.63$ Å, and $c = 5.41$ Å and average local magnetic moment for Co and Fe ions of $\mu_{Co} = 3.00\ \mu_B$ and $\mu_{Fe} = 4.10\ \mu_B$, respectively. However, the lattice parameters are strongly dependent to the local magnetic moment of Co (μ_{Co}). For $\mu_{Co} = 0\ \mu_B$, the structure keeps an AFM ordering in the Fe sublattice, and the theoretical lattice parameters change to $a = 5.44$ Å, $b = 7.61$ Å, and $c = 5.37$ Å, in good agreement with the observed room-temperature lattice parameters shown in Table 1. The energy difference between these two magnetic configurations, that is, with $\mu_{Co} = 3.00\ \mu_B$ and $\mu_{Co} = 0\ \mu_B$ is only 15 meV/f.u.

To simulate the conventional high temperature PM state of Nd_2CoFeO_6, we considered that the spins are randomly distributed over the lattice sites, including two constrains: (i) the total magnetic moment for the supercell is equal to zero; (ii) the total sum of local magnetic moments in each sublattice (Fe and Co) is set to zero. We carried out a systematic analysis with different initial magnetic moments for the Fe and Co atoms. For Fe atoms, starting with 4.00 μ_B as the local magnetic moment, μ_{Co} was allowed to vary between 0 and 3 μ_B. We tested a total of six different initial configurations in the PM state of the Nd_2CoFeO_6 compound. The relative stability of these configurations, as a function of the average Co local magnetic moment, along with the corresponding magnetic lattice representation are shown in Figure 3. The most stable PM configuration (low-T PM) has the average Co local magnetic moment close to 0; the stability of the system decreases as the local Co spin moment increases. Nevertheless, the total-energy difference between the most stable PM configuration and the lowest stable configuration (high-T PM) is lower than 70 meV/f.u, corresponding to 2.7 k_BT, with k_B the Boltzmann constant and $T = 293$ K. Also, this energy difference is of the same order of the energy separation between LS and HS states for single perovskites (30−80 meV).[53−55] This is a clear indication that, in the PM state, one should expect Co ions with LS configuration at low temperatures and a transition to the HS state at higher temperatures, in agreement with the experimental observations.

3.3. Electrical Transport and Band Structure Calculations. Because in many families of oxides spin, lattice, and

https://dx.doi.org/10.1021/acs.jpcc.0c07585
J. Phys. Chem. C 2020, 124, 22733−22742

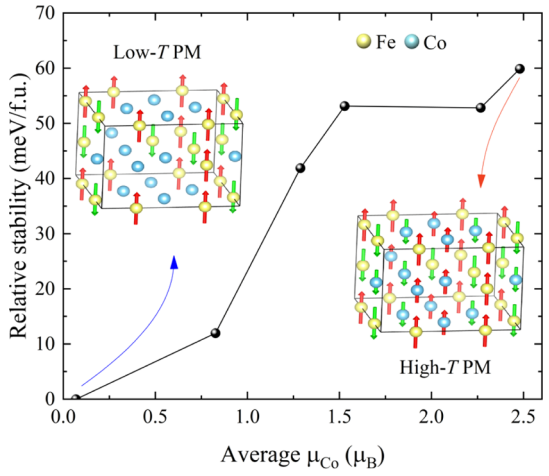

Figure 3. Relative stability of the PM phase as a function of the average local moment μ_{Co}. The low-T PM phase is the most stable configuration with the Co atoms in the LS state ($S = 0$). An increase in μ_{Co} has a negligible influence in the relative stability of the system, indicating that one should expect a thermally induced Co spin-state crossover in the high-T PM phase. The unit-cell arrows indicate the spin direction.

charge degrees of freedom are strongly coupled, temperature-dependent impedance spectroscopy was performed to correlate the charge transport and its possible relation to spin and lattice degrees of freedom. The main advantage of this technique is the separation among inductive (Z''), capacitive ($-Z''$), and resistive (Z') contributions for different relaxation processes in the grain, grain boundaries, and at interfaces. The most representative Nyquist plots are shown in Figure 4. The presence of a single semicircle arc at high frequencies indicates the relaxation comes just from bulk (intragrain contribution, $C \approx 10^{-12}$ to 10^{-11} F).[56] In this way, the equivalent circuit model was simulated considering just one resistance in parallel with

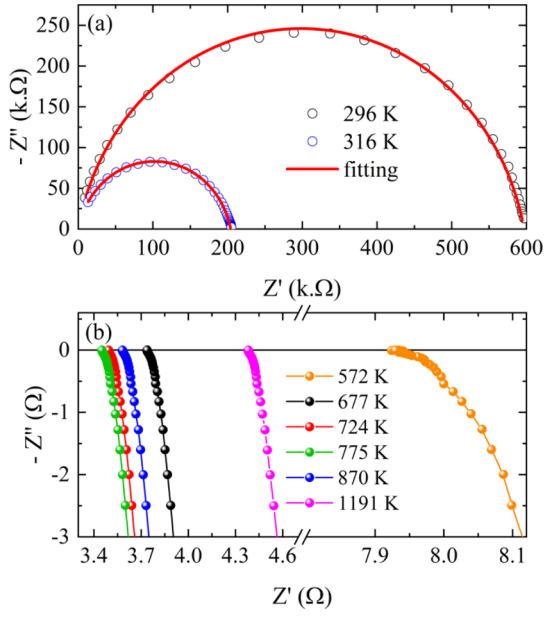

Figure 4. (a) Nyquist plot of Nd_2CoFeO_6 at 296 and 316 K along with respective fittings. (b) Nyquist plot in the high temperature regime where an inductive behavior is observed followed by an insulator-metal transition.

one constant phase element to account for the non-Debye relaxation, that is, distribution of characteristic relaxation frequencies. This model fits well with the experimental impedance spectra as shown in Figure 4a. For $T > 572$ K, the capacitive contribution in the semicircle is vanished and an inductive behavior is observed as shown in Figure 4b.

The temperature of this transition is close to the observed T_{PM} where a conventional PM state is achieved. For each temperature in this regime, the electrical resistance was obtained when the impedance spectra intercept the real axis, that is, at $\omega = 0$.[57] A huge decrease in electrical resistivity was noted, of about 6 order of magnitude until the system start to behave as a metal, as shown in Figure 5, revealing the presence

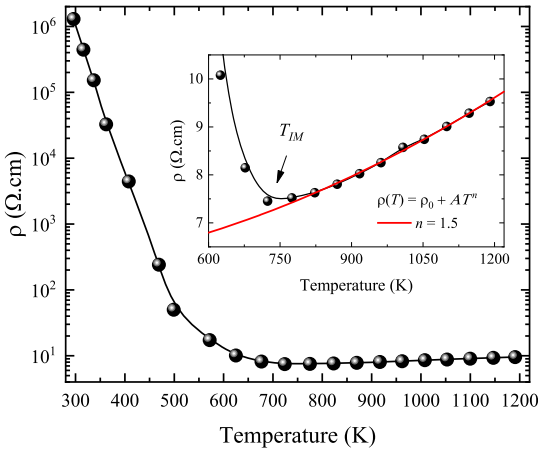

Figure 5. Temperature dependence of electrical resistivity obtained at $\omega = 0$ The inset highlights an insulator-metal transition for $T > 724$ K. The fitting above T_{IM} indicates an unusual metallic state, which might be related to electron−electron and electron-phonon scattering events.

of an IM transition temperature (T_{IM}). The decrease in the electrical resistance saturates at $T_{IM} = 724$ K corresponding to 7.61 Ω.cm. Above T_{IM}, the sign of $d\rho/dT$ is positive, thus indicating a crossover from insulating to a metallic-like behavior very close to the temperature interval where magnetic fluctuations show up. The inset of Figure 5 highlights an almost linear temperature dependency in the electrical resistivity above T_{IM}, indicating a faster energy dissipation than a conventional metal.

For a quantitative analysis of the metallic state, the electrical resistivity above T_{IM} was fitted by $\rho(T) = \rho_0 + AT^n$, where ρ_0 stands for the residual resistivity, and AT^n is related to distinct types of electron scatterings depending on the value of the exponent n.[58,59] In general, for a metal at the Fermi-liquid regime in the PM state there is a $\rho(T) \propto T^2$ dependency due to electron−electron scattering. On the other hand, for $n < 2$ anomalous metallic properties or, the non-Fermi liquid (NFL) behavior is manifested. As shown in the inset of Figure 5, the best fitting yields $n = 1.5$, which implies a NFL behavior of the high-T PM state, which we attribute to a combination of electron−electron and electron-phonon scatterings.[60] This indicates that Nd_2CoFeO_6 displays a bad-metal electrical conductivity at high temperatures. Interestingly, such an insulating to metal crossover is not followed by a structural phase transition as previously discussed. Recently, Tanwar et al.[10] and Cui et al.[61] reported high temperature transport properties of $La_{2-x}Sr_xCoFeO_6$ and $Ca_xY_{1-x}Fe_{0.5}Co_{0.5}O_{3-\delta}$. In

https://dx.doi.org/10.1021/acs.jpcc.0c07585
J. Phys. Chem. C 2020, 124, 22733−22742

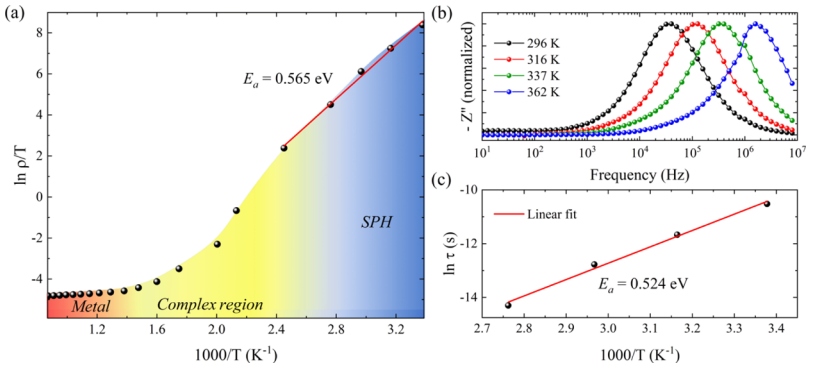

Figure 6. (a) Variation of $\ln(\rho/T)$ vs $1000/T$ for Nd_2CoFeO_6. One can distinguish three singular regions in the studied temperature range: a region that follows the SPH mechanism, a complex region where thermally induced Co spin-state transition took place, and a metallic region. (b) Frequency variation of the imaginary part of the impedance at different temperatures. (c) Temperature dependency of the relaxation frequency according to the Arrhenius law.

the former, the resistivity did not show any sign of T_{IM} for $x <$ 0.4 up to 1100 K, and in the latter the absence for T_{IM} was observed up to 700 K.

To analyze the conduction mechanism in the insulating regime, we considered both $\rho(T)$ and $-Z''(f)$ of the complex impedance. In the first case, $\rho(T)$ was fitted by a small polaron hopping (SPH) conduction model. Usually, localized carriers are expected to polarize the ions in their neighborhood and distort the surrounding lattice exchanging energy and forming a small bounded polaron with an extension comparable with a lattice spacing. The linear fitting, shown in Figure 6a, results in an activation energy E_a = 0.565 eV. However, at the intermediate insulating temperature range (410 K < T < 724 K), the experimental data starts to deviate from the SPH model probably because of local magnetic fluctuations as observed before. As far as this point is concerned, the presence of magnetic ions with fluctuations in the spin state as the temperature increases cannot be captured by the polaron model. This must be a very complex transport mechanism phenomenon. Indeed, a closed analytical expression for the temperature dependence of the electrical transport including changing in the spin state is not available. The addition of spin-state transitions tangles the transport properties leading to difficulties in our fundamental understanding of the conduction mechanism. Furthermore, as the temperature is increased, the presence of defects may also lead to contribution of ionic conductivity related to mobility of oxygen vacancies. Also, the dynamic relaxation of charge carriers was taken into consideration as shown in Figure 6b. The presence of a single peak at high frequencies denote a bulk relaxation process as discussed before. The peak shifts to higher frequencies as the temperatures rises, which indicates that the charge transport mechanism is thermally activated. The temperature dependence of the relaxation time for intragrain contribution is expected by the Arrhenius relation $\tau = \tau_0 \exp(-E_a/k_BT)$, where τ_0 is a pre-exponential factor and E_a is the activation energy, k_B is the Boltzmann constant, and T is the absolute temperature. In Figure 6c, the linear fitting of the experimental data indicates an activation energy of E_a = 0.524 eV.

The experimental results above clearly indicate that the increase in temperature leads to two important changes in the physical properties of the Nd_2CoFeO_6 compound. First, a PM transition is observed and correlated to the change in the local moments on the Co atoms. The second observation is the complete melting of polaronic insulating regime toward a metallic conductivity. It is interesting to mention that there is strong evidence that change in the cooperative nature of the local distortions and long-range elastic field is responsible for changes in the strength of the charge-lattice coupling forming polarons.[62] In this line, electronic phase transition from a polaronic liquid to a polaronic gas can be driven by the average lattice symmetry.[63] Here, the polaron melting takes place in the absence of structural phase transitions indicating that other mechanisms are playing a role. On the other hand, our first principle calculations show how these two transitions are connected and directly related to the change in the Co magnetic moment.

First-principles calculations were then used to understand the electronic structure of the Nd_2CoFeO_6 compound. In Figure 7, we show the variation of the band gap (E_g) as function of the average local Co magnetic moment inside the PM supercell. We find an almost linear behavior, with largest E_g for the LS configurations of the Co local magnetic moment, and a metal system (E_g = 0) for a HS configuration on the Co atoms. Therefore, our results show that the increase in the local magnetic moment of Co ions in a PM state is related to

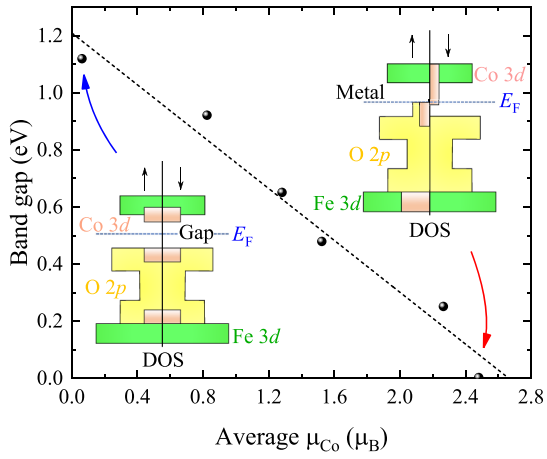

Figure 7. Band gap energy as function of the average local magnetic moment of Co for the paramagnetic configuration. As the μ_{Co} increases, the band structure tends to a gapless state by the merge between unoccupied Co 3d orbitals and the occupied O 2p orbitals. The dashed line indicates a linear relationship between E_g and μ_{Co}. The diagrams schematically indicate the change on the relevant levels as explicitly shown in Figure 8.

https://dx.doi.org/10.1021/acs.jpcc.0c07585
J. Phys. Chem. C 2020, 124, 22733−22742

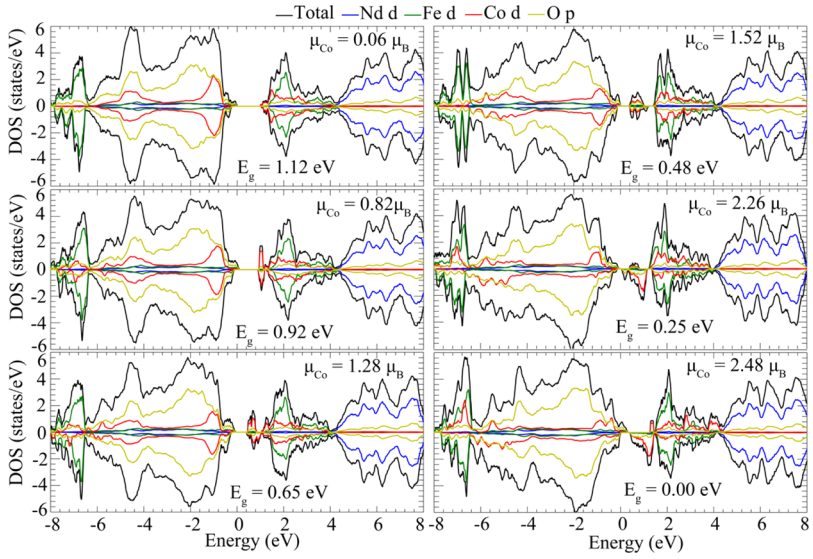

Figure 8. Orbital projected density of states for the Nd_2CoFeO_6 compound in the paramagnetic configuration. Each panel indicates a different average local magnetic moment of Co atoms and its band gap; it increases in the following sequence: top to bottom and left to right. The increase in the local magnetic moments of Co atoms induces a decrease in the band gap.

an IM transition, in agreement with the IM transition observed at high temperature, as shown in Figure 5. Although DFT within the generalized gradient approximation typically underestimates the fundamental band gap energy for semiconductors and insulators,[64] we expect the observed linear behavior of the band gap as function of Co local magnetic moment to be qualitative correct. We note that the value of U_{eff} in DFT + U changes the inclination of the line, affecting the DFT potential energy surface. For a small U_{eff}, the local wells in the potential energy surface are not so deep, resulting in slight variations of Co magnetic moment, leading to instabilities when in the convergence of the calculations.

We also computed the density of states for each PM configuration, the results are shown in Figure 8, with the Fermi level set to 0 eV. For all systems considered, the valence band is composed mainly by O 2p orbitals hybridized with Co 3d. The occupied Fe 3d orbitals are located at ≈7 eV below the Fermi level. In contrast, the conduction shows small contribution from of Co 3d orbitals, and the unoccupied Fe 3d orbitals are localized around 0.5 eV above the conduction band minimum (CBM) for the most stable PM structure, as shown in the right-top panel of Figure 8. These represent the configurations with the smallest Co local magnetic moments. When the average of local Co magnetic moment increases, the band gap energy decreases because the enhancement and delocalization of the unoccupied Co 3d orbitals in the vicinity of CBM. At the same time, the hybridization between the O 2p and Co 3d close to the valence band maximum (VBM) decreases while that between Fe 3d and Co 3d increases at deep energies (≈7 eV). For large Co local magnetic moments, the band gap vanishes because of the merging of unoccupied Co 3d orbitals and the occupied O 2p orbitals, resulting in a metallic system.

The variation in the local magnetic moment of Co ions also leads to changes in the lattice parameters. As discussed above, as seen Figure 5b, the a-axis shows a small step variation at high temperature close to the IM transition. In our calculations, we observe a variation of 2.5% in the lattice parameter a from the insulating (low average Co magnetic moment) to the metallic phase (high average Co magnetic moment) of the paramagnetic Nd_2CoFeO_6 compound. The b and c lattice parameters are not so sensitive to the variation of the Co local magnetic moment, leading to a maximum increase of 0.6%, in agreement with the experimental observations. Therefore, our calculations clearly show that both the IM transition and the lattice parameter increase are correlated to a change in the Co spin state. In the calculations, each spin state corresponds to a local minimum in the complex potential energy surface that is experimentally reachable through the increase in temperature. The complex hybridization between Co 3d and O 2p orbitals seem responsible to the changes in band dispersions that lead to the metallic states.

4. CONCLUSIONS

In summary, we report the structural, magnetic, and electronic transport properties of Nd_2CoFeO_6 as a novel disordered double perovskite compound. A close connection among lattice, spin, and charge transport properties is confirmed by both experimental and theorical approaches. A huge decrease in the electrical resistivity is followed by an unambiguous transition from insulating polaronic regime down to a well-defined metallic-like state at high temperatures. This electronic crossover occurring in the paramagnetic state provides an ideal scenario for a better understanding of the evolution of the polaronic behavior through different spin states. Analysis of the insulating polaronic regime indicates activation energy around 0.5 eV. We show by special quasirandom structures simulations that the paramagnetic configurations have a direct relation to this crossover due to transitions from low to high spin states of Co^{3+} ions increasing the local magnetic moment in the magnetic lattice. Our results point to a scenario in which a continuous spin-state transition triggers a crossover to a gapless state due to a complex hybridization of unoccupied Co 3d orbitals and the occupied O 2p orbitals states. We hope that our results bring advances on the fundamental understanding of this complex system where structural, magnetic, and electronic properties are strongly coupled.

https://dx.doi.org/10.1021/acs.jpcc.0c07585
J. Phys. Chem. C 2020, 124, 22733−22742

■ ASSOCIATED CONTENT

Supporting Information

The Supporting Information is available free of charge at https://pubs.acs.org/doi/10.1021/acs.jpcc.0c07585.

Influence of calcination temperature in the sample of Nd_2O_3 and magnetic field-dependent isothermal magnetization (PDF)

■ AUTHOR INFORMATION

Corresponding Author

Jose A. Souza − *Federal University of ABC, Santo André, São Paulo 09210-580, Brazil;* orcid.org/0000-0002-6832-3581; Email: joseantonio.souza@ufabc.edu.br

Authors

Leonardo S. de Oliveira − *Federal University of ABC, Santo André, São Paulo 09210-580, Brazil;* orcid.org/0000-0001-9999-206X

Fernando P. Sabino − *Federal University of ABC, Santo André, São Paulo 09210-580, Brazil*

Daniel Z. de Florio − *Federal University of ABC, Santo André, São Paulo 09210-580, Brazil;* orcid.org/0000-0002-7291-1917

Anderson Janotti − *Department of Materials Science and Engineering, University of Delaware, Newark, Delaware 19716, United States;* orcid.org/0000-0002-0358-2101

Gustavo M. Dalpian − *Federal University of ABC, Santo André, São Paulo 09210-580, Brazil;* orcid.org/0000-0001-5561-354X

Complete contact information is available at: https://pubs.acs.org/10.1021/acs.jpcc.0c07585

Author Contributions

The manuscript was written through equally contribution of all authors. All authors have given approval to the final version of the manuscript.

Notes

The authors declare no competing financial interest.

■ ACKNOWLEDGMENTS

This work was conducted during a PhD scholarship financed by the CAPES—Brazilian Federal Agency for Support and Evaluation of Graduate Education. This work is supported by the Brazilian agency CNPq under grants no. 307950/2017-4, 404951/2016-3, 309600/2018-9, and 303552/2016-6 and by the FAPESP under grants no. 2017/02317-2, 2018/15682-3, 2015/24999-2, and 2019/21656-8. A.J. was supported by the NSF Faculty Early Career Development Program DMR-1652994. The authors are grateful to the CEM − Multiuser Experimental Center of UFABC. *Ab initio* calculations were performed at the LNCC supercomputer center (Santos Dumont).

■ ABBREVIATIONS

ASD,antisite disorder; IM,insulator−metal; PM,paramagnetic; SQS,special quasirandom structure; XRD,X-ray diffraction; ZFC,zero field cooled; FC,field cooled; PAW,projected augmented waves; DFT,density functional theory; DOS,density of states; AFM,antiferromagnetic; FM,ferromagnetic; CW,Curie−Weiss; HS,high spin; IS,intermediate spin; LS,low spin; SS,spin state; NFL,non-fermi liquid; SPH,small polaron hopping; CBM,conduction band minimum; VBM,valence band maximum

■ REFERENCES

(1) *Colossal Magnetoresistive Oxides*, 1st ed.; Tokura, Y., Ed.; CRC Press, 2000.

(2) Dagotto, E.; Hotta, T.; Moreo, A. Colossal Magnetoresistant Materials: The Key Role of Phase Separation. *Phys. Rep.* **2001**, *344*, 1−153.

(3) Vasala, S.; Karppinen, M. $A_2B'B''O_6$ Perovskites: A Review. *Prog. Solid State Chem.* **2015**, *43*, 1−36.

(4) Viola, M. C.; Martínez-Lope, M. J.; Alonso, J. A.; Martínez, J. L.; De Paoli, J. M.; Pagola, S.; Pedregosa, J. C.; Fernández-Díaz, M. T.; Carbonio, R. E. Structure and Magnetic Properties of Sr_2CoWO_6: An Ordered Double Perovskite Containing Co^{2+} (HS) with Unquenched Orbital Magnetic Moment. *Chem. Mater.* **2003**, *15*, 1655−1663.

(5) Mishra, R.; Soliz, J. R.; Woodward, P. M.; Windl, W. Ca2MnRuO6: Magnetic Order Arising from Chemical Chaos. *Chem. Mater.* **2012**, *24*, 2757−2763.

(6) Morrow, R.; Mishra, R.; Restrepo, O. D.; Ball, M. R.; Windl, W.; Wurmehl, S.; Stockert, U.; Büchner, B.; Woodward, P. M. Independent Ordering of Two Interpenetrating Magnetic Sublattices in the Double Perovskite Sr_2CoOsO_6. *J. Am. Chem. Soc.* **2013**, *135*, 18824−18830.

(7) Li, Y.; Cheng, J.; Song, J.; Alonso, J. A.; Fernández-Díaz, M. T.; Goodenough, J. B. Characterization of the Double Perovskite $Ba_2Bi_xSc_{0.2}Co_{1.8-x}O_{6-\delta}$ (x = 0.1, 0.2). *Chem. Mater.* **2012**, *24*, 4114−4122.

(8) Huang, Y. H.; Karppinen, M.; Yamauchi, H.; Goodenough, J. B. Systematic Studies on Effects of Cationic Ordering on Structural and Magnetic Properties in Sr 2 FeMoO 6. *Phys. Rev. B: Condens. Matter Mater. Phys.* **2006**, *73*, 104408.

(9) Menéndez, N.; García-Hernández, M.; Sánchez, D.; Tornero, J. D.; Martínez, J. L.; Alonso, J. A. Charge Transfer and Disorder in Double Perovskites. *Chem. Mater.* **2004**, *16*, 3565−3572.

(10) Tanwar, K.; Gyan, D. S.; Bhattacharya, S.; Vitta, S.; Dwivedi, A.; Maiti, T. Enhancement of Thermoelectric Power Factor by Inducing Octahedral Ordering in $La_{2-x}Sr_xCoFeO_6$ Double Perovskites. *Phys. Rev. B* **2019**, *99*, 174105.

(11) Shukla, A.; Singh, A.; Seikh, M. M.; Kundu, A. K. Low Temperature Magneto-Dielectric Coupling in Nanoscale Layered $SmFe_{0.5}Co_{0.5}O_3$ Perovskite. *J. Phys. Chem. Solids* **2019**, *127*, 164−168.

(12) Haripriya, G. R.; Pradheesh, R.; Singh, M. N.; Sinha, A. K.; Sethupathi, K.; Sankaranarayanan, V. Temperature Dependent Structural Studies on the Spin Correlated System A_2FeCoO_6 (A= Sm, Eu, Dy and Ho) Using Synchrotron Radiation. *AIP Adv.* **2017**, *7*, 055826.

(13) Lohr, J.; Pomiro, F.; Pomjakushin, V.; Alonso, J. A.; Carbonio, R. E.; Sánchez, R. D. Multiferroic Properties of $RFe_{0.5}Co_{0.5}O_3$ with R = Tm , Er, Ho, Dy, and Tb. *Phys. Rev. B* **2018**, *98*, 134405.

(14) Shukla, A.; Lebedev, O. I.; Seikh, M. M.; Kundu, A. K. Structural and Magnetic Characterization of Spin Canted Mixed Ferrite-Cobaltites: $LnFe_{0.5}Co_{0.5}O_3$ (Ln = Eu and Dy). *J. Magn. Magn. Mater.* **2019**, *491*, 165558.

(15) Das, M.; Mandal, P. Nonlinear Magnetodielectric and Magnetocaloric Properties of Double Perovskite Ho_2FeCoO_6. *Phys. B Condens. Matter* **2019**, *571*, 32−35.

(16) Dong, Z.; Yin, S. Structural, Magnetic and Magnetocaloric Properties in Perovskite RE_2FeCoO_6 (RE = Er and Gd) Compounds. *Ceram. Int.* **2020**, *46*, 1099.

(17) Pal, A.; Singh, P.; Gangwar, V. K.; Ghosh, S.; Prakash, P.; Saha, S. K.; Das, A.; Kumar, M.; Ghosh, A. K.; Chatterjee, S. B-Site Disorder Driven Multiple-Magnetic Phases: Griffiths Phase, Re-Entrant Cluster Glass, and Exchange Bias in Pr_2CoFeO_6. *Appl. Phys. Lett.* **2019**, *114*, 252403.

(18) Rietveld, H. M. A Profile Refinement Method for Nuclear and Magnetic Structures. *J. Appl. Crystallogr.* **1969**, *2*, 65−71.

(19) Larson, A. C.; Von Dreele, R. B. *General Structure Analysis System (GSAS); Los Alamos National Laboratory Report LAUR*, 2004; pp 86−748.
(20) McCusker, L. B.; Von Dreele, R. B.; Cox, D. E.; Louër, D.; Scardi, P. Rietveld Refinement Guidelines. *J. Appl. Crystallogr.* **1999**, *32*, 36−50.
(21) Kresse, G.; Hafner, J. *Ab Initio* Molecular Dynamics for Open-Shell Transition Metals. *Phys. Rev. B: Condens. Matter Mater. Phys.* **1993**, *48*, 13115−13118.
(22) Kresse, G.; Furthmüller, J. Efficient Iterative Schemes for *Ab Initio* Total-Energy Calculations Using a Plane-Wave Basis Set. *Phys. Rev. B: Condens. Matter Mater. Phys.* **1996**, *54*, 11169−11186.
(23) Perdew, J. P.; Ruzsinszky, A.; Csonka, G. I.; Vydrov, O. A.; Scuseria, G. E.; Constantin, L. A.; Zhou, X.; Burke, K. Restoring the Density-Gradient Expansion for Exchange in Solids and Surfaces. *Phys. Rev. Lett.* **2008**, *100*, 136406.
(24) Blöchl, P. E. Projector Augmented-Wave Method. *Phys. Rev. B: Condens. Matter Mater. Phys.* **1994**, *50*, 17953−17979.
(25) Kresse, G.; Joubert, D. From Ultrasoft Pseudopotentials to the Projector Augmented-Wave Method. *Phys. Rev. B: Condens. Matter Mater. Phys.* **1999**, *59*, 1758−1775.
(26) Dudarev, S. L.; Botton, G. A.; Savrasov, S. Y.; Humphreys, C. J.; Sutton, A. P. Electron-Energy-Loss Spectra and the Structural Stability of Nickel Oxide: An LSDA+U Study. *Phys. Rev. B: Condens. Matter Mater. Phys.* **1998**, *57*, 1505−1509.
(27) Zunger, A.; Wei, S.-H.; Ferreira, L. G.; Bernard, J. E. Special Quasirandom Structures. *Phys. Rev. Lett.* **1990**, *65*, 353−356.
(28) Wei, S.-H.; Ferreira, L. G.; Bernard, J. E.; Zunger, A. Electronic Properties of Random Alloys: Special Quasirandom Structures. *Phys. Rev. B: Condens. Matter Mater. Phys.* **1990**, *42*, 9622−9649.
(29) Malyi, O. I.; Dalpian, G. M.; Zhao, X.-G.; Wang, Z.; Zunger, A. Realization of Predicted Exotic Materials: The Burden of Proof. *Mater. Today* **2020**, *32*, 35−45.
(30) Pomiro, F.; Gil, D. M.; Nassif, V.; Paesano, A.; Gómez, M. I.; Guimpel, J.; Sánchez, R. D.; Carbonio, R. E. Weak Ferromagnetism and Superparamagnetic Clusters Coexistence in YFe1−xCoxO3 (0≤x≤1) Perovskites. *Mater. Res. Bull.* **2017**, *94*, 472−482.
(31) Yadav, R.; Elizabeth, S. Magnetic Frustration and Dielectric Relaxation in Insulating Nd_2NiMnO_6 Double Perovskites. *J. Appl. Phys.* **2015**, *117*, 053902.
(32) Sławiński, W.; Przeniosło, R.; Sosnowska, I.; Suard, E. Spin Reorientation and Structural Changes in $NdFeO_3$. *J. Phys.: Condens. Matter* **2005**, *17*, 4605−4614.
(33) Yuan, S.; Wang, Y.; Shao, M.; Chang, F.; Kang, B.; Isikawa, Y.; Cao, S. Magnetic Properties of $NdFeO_3$ Single Crystal in the Spin Reorientation Region. *J. Appl. Phys.* **2011**, *109*, 07E141.
(34) Souza, J. A.; Neumeier, J. J.; Jardim, R. F. Effect of Disorder on the Thermodynamic Phase Transition in La0.70Ca0.30MnO3. *Phys. Rev. B: Condens. Matter Mater. Phys.* **2007**, *75*, 012412.
(35) Retuerto, M.; Li, M.-R.; Stephens, P. W.; Sánchez-Benítez, J.; Deng, X.; Kotliar, G.; Croft, M. C.; Ignatov, A.; Walker, D.; Greenblatt, M. Half-Metallicity in Pb_2CoReO_6 Double Perovskite and High Magnetic Ordering Temperature in Pb2CrReO6 Perovskite. *Chem. Mater.* **2015**, *27*, 4450−4458.
(36) Schiffer, P.; Daruka, I. Two-Population Model for Anomalous Low-Temperature Magnetism in Geometrically Frustrated Magnets. *Phys. Rev. B: Condens. Matter Mater. Phys.* **1997**, *56*, 13712−13715.
(37) Garcia, F. A.; Kaneko, U. F.; Granado, E.; Sichelschmidt, J.; Hölzel, M.; Duque, J. G. S.; Nunes, C. A. J.; Amaral, R. P.; Marques-Ferreira, P.; Lora-Serrano, R. Magnetic Dimers and Trimers in the Disordered S = 3/2 Spin System BaTi1/2Mn1/2O3. *Phys. Rev. B: Condens. Matter Mater. Phys.* **2015**, *91*, 224416.
(38) Bray, A. J. Nature of the Griffiths Phase. *Phys. Rev. Lett.* **1987**, *59*, 586−589.
(39) Bray, A. J. Dynamics of Dilute Magnets above Tc. *Phys. Rev. Lett.* **1988**, *60*, 720−723.
(40) Griffiths, R. B. Nonanalytic Behavior Above the Critical Point in a Random Ising Ferromagnet. *Phys. Rev. Lett.* **1969**, *23*, 17−19.
(41) Galdino, C. W.; Freitas, D. C.; Medrano, C. P. C.; Tartaglia, R.; Rigitano, D.; Oliveira, J. F.; Mendonça, A. A.; Ghivelder, L.; Continentino, M. A.; Sanchez, D. R.; Granado, E. Magnetic, Electronic, Structural, and Thermal Properties of the Co 3 O 2 BO 3 Ludwigite in the Paramagnetic State. *Phys. Rev. B* **2019**, *100*, 165138.
(42) Souza, J. A.; Neumeier, J. J.; Yu, Y.-K. Magnetic Signatures of Ferromagnetic Polarons in La0.7Ca0.3MnO3 : Colossal Magnetoresistance Is Not a Griffiths Singularity. *Phys. Rev. B: Condens. Matter Mater. Phys.* **2008**, *78*, 014436.
(43) Karpinsky, D. V.; Troyanchuk, I. O.; Bärner, K.; Szymczak, H.; Tovar, M. Crystal Structure and Magnetic Ordering of the $LaCo_{1-x}$ Fe x O_3 Sy$_s$tem. *J. Phys.: Condens. Matter* **2005**, *17*, 7219−7226.
(44) Zobel, C.; Kriener, M.; Bruns, D.; Baier, J.; Grüninger, M.; Lorenz, T.; Reutler, P.; Revcolevschi, A. Evidence for a Low-Spin to Intermediate-Spin State Transition in LaCoO 3. *Phys. Rev. B: Condens. Matter Mater. Phys.* **2002**, *66*, 020402.
(45) Yan, J.-Q.; Zhou, J.-S.; Goodenough, J. B. Bond-Length Fluctuations and the Spin-State Transition in L CoO 3 (L = La , Pr, and Nd). *Phys. Rev. B: Condens. Matter Mater. Phys.* **2004**, *69*, 134409.
(46) Goodenough, J. B. An Interpretation of the Magnetic Properties of the Perovskite-Type Mixed Crystals La1−xSrxCoO3−λ. *J. Phys. Chem. Solids* **1958**, *6*, 287−297.
(47) Huang, X.; Zhang, W. How Does the Spin-State of Co Ions Affect the Insulator-Metal Transition in Bi2A2Co2O8 (A = Ca, Sr, Ba)? *Sci. Rep.* **2016**, *6*, 38212.
(48) Wu, H. Metal-Insulator Transition in Sr2−xLaxCoO 4 Driven by Spin-State Transition. *Phys. Rev. B: Condens. Matter Mater. Phys.* **2012**, *86*, 075120.
(49) Korotin, M. A.; Ezhov, S. Y.; Solovyev, I. V.; Anisimov, V. I.; Khomskii, D. I.; Sawatzky, G. A. Intermediate-Spin State and Properties of LaCoO3. *Phys. Rev. B: Condens. Matter Mater. Phys.* **1996**, *54*, 5309−5316.
(50) Lubinskii, N. N.; Bashkirov, L. A.; Galyas, A. I.; Shevchenko, S. V.; Petrov, G. S.; Sirota, I. M. Magnetic Susceptibility and Effective Magnetic Moment of the Nd3+ and Co3+ Ions in NdCo1−xGaxO3. *Inorg. Mater.* **2008**, *44*, 1015−1021.
(51) Haverkort, M. W.; Hu, Z.; Cezar, J. C.; Burnus, T.; Hartmann, H.; Reuther, M.; Zobel, C.; Lorenz, T.; Tanaka, A.; Brookes, N. B.; Hsieh, H. H.; Lin, H.-J.; Chen, C. T.; Tjeng, L. H. Spin State Transition in LaCoO3 Studied Using Soft X-Ray Absorption Spectroscopy and Magnetic Circular Dichroism. *Phys. Rev. Lett.* **2006**, *97*, 176405.
(52) Craco, L.; Müller-Hartmann, E. Dynamical Correlations across the Spin-State Transition in LaCoO3. *Phys. Rev. B: Condens. Matter Mater. Phys.* **2008**, *77*, 045130.
(53) Yamaguchi, S.; Okimoto, Y.; Taniguchi, H.; Tokura, Y. Spin-State Transition and High-Spin Polarons in LaCoO3. *Phys. Rev. B: Condens. Matter Mater. Phys.* **1996**, *53*, R2926−R2929.
(54) Aswin, V.; Dogra, A.; Gupta, A.; Pulikkotil, J. J. Retentivity of Spin State Transitions in $LaCoO_3$ with Chemical Disorder. *RSC Adv.* **2016**, *6*, 1403−1407.
(55) Ovchinnikov, S. G.; Orlov, Y. S.; Dudnikov, V. A. Temperature and Field Dependent Electronic Structure and Magnetic Properties of LaCoO3 and GdCoO3. *J. Magn. Magn. Mater.* **2012**, *324*, 3584−3587.
(56) Irvine, J. T. S.; Sinclair, D. C.; West, A. R. Electroceramics: Characterization by Impedance Spectroscopy. *Adv. Mater.* **1990**, *2*, 132−138.
(57) Jonscher, A. K. The 'Universal' Dielectric Response. *Nature* **1977**, *267*, 673−679.
(58) Hossain Khan, M.; Pal, S.; Bose, E. Metal-Insulator Transition and Non-Adiabatic Small Polaron Hopping Conduction in Electron-Doped Ca $_{0.85}$ Pr $_{0.15}$ MnO $_3$ Manganite. *Phys. Scr.* **2015**, *90*, 035803.
(59) Mikheev, E.; Hauser, A. J.; Himmetoglu, B.; Moreno, N. E.; Janotti, A.; Van de Walle, C. G.; Stemmer, S. Tuning Bad Metal and Non-Fermi Liquid Behavior in a Mott Material: Rare-Earth Nickelate Thin Films. *Sci. Adv.* **2015**, *1*, No. e1500797.

https://dx.doi.org/10.1021/acs.jpcc.0c07585
J. Phys. Chem. C 2020, 124, 22733−22742

(60) Blasco, J.; Garcia, J. A Comparative Study of the Crystallographic, Magnetic and Electrical Properties of the Nd $_{1-x}$ La $_{x}$ NiO $_{3-\ delta}$ System. *J. Phys.: Condens. Matter* **1994**, *6*, 10759−10772.
(61) Cui, J.; Wang, J.; Zhang, X.; Li, G.; Wu, K.; Cheng, Y.; Zhou, J. Enhanced Oxygen Reduction Reaction through Ca and Co Co-Doped $YFeO_3$ as Cathode for Protonic Ceramic Fuel Cells. *J. Power Sources* **2019**, *413*, 148−157.
(62) Khomskii, D. I.; Kugel, K. I. Elastic Interactions and Superstructures in Manganites and Other Jahn-Teller Systems. *Phys. Rev. B: Condens. Matter Mater. Phys.* **2003**, *67*, 134401.
(63) Souza, J. A.; Terashita, H.; Granado, E.; Jardim, R. F.; Oliveira, N. F.; Muccillo, R. Polaron Liquid-Gas Crossover at the Orthorhombic-Rhombohedral Transition of Manganites. *Phys. Rev. B: Condens. Matter Mater. Phys.* **2008**, *78*, 054411.
(64) Perdew, J. P. Density Functional Theory and the Band Gap Problem. *Int. J. Quantum Chem.* **2009**, *28*, 497−523.

https://dx.doi.org/10.1021/acs.jpcc.0c07585
J. Phys. Chem. C 2020, 124, 22733−22742